Multi-hazard assessment in Europe under climate change

Supplementary Material

Giovanni Forzieri, Luc Feyen, Simone Russo, Michalis Vousdoukas, Lorenzo Alfieri, Stephen Outten, Mirco Migliavacca, Alessandra Bianchi, Rodrigo Rojas, Alba Cid

Correspondence: Corresponding author: Giovanni Forzieri, European Commission, Joint Research Centre (JRC), Institute for Environment and Sustainability (IES), Climate Risk Management Unit, Via Enrico Fermi 2749, 21027 Ispra VA, Italy (giovanni.forzieri@jrc.ec.europa.eu); tel: +39 0332785528; fax: +39 0332786653.

Text S1. Modelling of climate hazards

The modelling approaches are briefly described in the following lines for each climate hazard; additional details can be found in the cited references. If not differently reported, the mentioned time slices refer to the baseline (1981-2010), 2020s (2011-2040), 2050s (2041-2070) and 2080s (2071-2100) and reference return periods of extreme events range between 2 and 100 years. Future climate hazards have been derived based on climate simulations from an ensemble of Global Circulation Model-Regional Climate Model (GCM-RCM) combinations under a "business-as-usual" (SRES A1B) greenhouse gas emissions trajectory (Solomon 2007) (Table S1). Precipitation and temperature fields utilized in our study as climatic drivers have been bias corrected by the quantile method (Dosio and Paruolo 2011). We used climate experiments corrected based on the quantile method because it showed better performance compared to other methods to correct for bias in high-resolution regional climate models (Jakob Themeßl et al. 2011). Improvements in both the upper and lower tail of the probability distribution functions (PDFs) of temperature and precipitation have been documented, with positive effects on the accuracy of simulated extreme climatic and hydrological events (Rojas et al. 2011; Dosio and Paruolo 2011).

Heat and cold waves. The Heat Wave Magnitude Index daily HWMId is defined as the maximum magnitude of the heat waves in a year, where heat wave is the period ≥ 3 consecutive days with maximum temperature above the daily threshold for the reference period 1981–2010. The threshold is defined as the 90th percentile of daily maxima, centered on a 31-day window for the reference period 1981-2010. The HWMId sums standardized excess temperatures beyond a certain normalized threshold and merges durations and temperature anomalies of intense heat wave events into a single number. The HWMId is defined in [0,+Inf[and it is the improvement of the previous Heat Wave Magnitude Index HWMI (Russo et al. 2014) able to overcome HWMI limitations in assigning magnitude to very high temperatures in a changing climate (Russo et al. 2015). Daily temperatures required for heat waves were retrieved in each 25km grid cell of the domain from five different GCM-RCM configurations under the A1B emission scenario (Table S1). Return levels of heat waves were computed by means of a kernel density estimator with triangular kernel separately for each time slice and climate experiment. In analogy to the heat waves, we have extended the methodology to quantify cold waves. Here cold waves are defined as

three consecutive days with daily minimum temperature below the daily threshold defined as the 10th percentile of daily minima, centred on a 31-day window. In analogy to the HWMId definition the Cold Wave Magnitude Index daily (CWMId) is defined as the minimum of the magnitude of all the cold waves in a year with values in]-Inf,0]. The CWMId sums the negative magnitude of the consecutive days composing a coldwave. The retrieval of CWMId return levels follows the same approach as describe for HWMId.

Wildfires. Simulations of wildfires were performed with the Community Land Model (CLM) based on the fire algorithm (Kloster et al. 2010) and optimized for application in Europe (Migliavacca et al. 2013b). CLM computes at each time step the total probability of fire occurrence as the product of three terms: the probability related to fuel, or biomass availability, the probability conditioned on the moisture and the probability of ignition. The last term is retrieved from the natural ignition (lightning) probability, the human-induced ignition probability and the human capacity of fire suppression. Human functional components are quantified by the use of empirical relations with population density as predictor. As final model output, the fraction of burned area is derived as a function of the total probability of fire occurrence, wind speed and soil moisture conditions. The model is parameterized on European datasets of soil properties, vegetation biophysical characteristics, population distribution and meteorological fields and validated at country level based on the European Forest Fires Information System (European Commission 2008) and the Global Fires Emission Database (Giglio et al. 2010; van der Werf et al. 2010). Simulations over the 21st century were obtained by forcing CLM with five different GCM-RCM combinations under the A1B emission scenario (Table S1). For each climate experiment, 120 years of monthly fraction of burned area (1981-2100) was produced at each grid cell (25km spatial resolution) and its spatial and temporal variations are described in an earlier work (Migliavacca et al. 2013a). Monthly fractions of burned area values were annually aggregated and three different functions (beta, gamma and GEV) were fitted through the annual fractions of burned area to derive extreme events. The beta function was selected because it better reflects the domain of the physical variable (fraction constrained by 0 and 1) and it showed the highest percentage of convergent pixels.

Windstorms. Wind fields were derived from a four-member ensemble GCM-RCM combinations under the A1B emission scenario (Table S1). For this hazard the baseline refers to the 1961-1990 period while the future scenario to the 2071-2100 period. Daily maximum

10m wind speed was selected at each 25km grid cell. Extreme events were calculated for each time slice using a peaks-over-threshold approach at each grid point independently, where the threshold used was the minimum of the annual maxima at that grid point. A maximum likelihood estimation method was used to fit the Generalized Pareto Distribution to the exceedances, after a simple declustering approach was used to ensure independence of the events (Outten and Esau 2013).

Coastal floods. Coastal floods were estimated taking into account three hourly components of the total water level: mean water level (MWL), storm surge (SS), astronomical tide (AT) and wave set-up. SS values were obtained by means of a numerical simulation using the ROMS model (Haidvogel et al. 2008) set up at a 7km spatial resolution in a barotropic mode to take into account non-linear effects. Tidal harmonic constants were extracted from the TPXO7.2 global model (Egbert and Erofeeva 2002) and then used to predict hourly astronomical tide levels (AT) at a spatial resolution of 0.25º. Hourly wave parameters were simulated using the WWIII v4.18 model (Hendrik Tolman 2014) at a spatial resolution of 0.125º and with multigrid two-way nesting in European near-shore areas (Reguero et al. 2012). Both ROMS and WWIII models were forced by wind and pressure fields from the CFSR reanalysis for the reference 1979-2014 period (Saha et al. 2010). The total water level (TWL) was obtained from the combination of the hourly time series of the 3 variables: TWL = $0.2*H_{sp}$ + SS + AT. Extremes of the TWL (return periods from 2 to 500 years) were obtained from a peak-over-threshold approach selecting a threshold which resulted in at least 5 events per year (Cid et al. 2014). Future TWL values were estimated by adding projections of A1B-consistent Relative Sea Level Rise (1981-2100) (Pardaens et al. 2011) to the present day TWL values. Following, TWL return period values were estimated along every 25 km of European coastline and a static inundation approach was applied in combination with a high resolution DEM, limiting the horizontal inundation extent to 50 km from the coast. Outcome of this procedure were 100-m spatial resolution inundation maps for each return period and time slice.

River floods and droughts. The LISFLOOD hydrological model was used to derive time series of daily river discharge at pan-European scale. LISFLOOD is a GIS-based hydrological model where processes such as infiltration, water consumption by plants, snowmelt, freezing of soils, surface runoff and groundwater storage are explicitly accounted for at the grid level (Van Der Knijff et al. 2010). Spatial properties for soils, vegetation types,

land uses, and river channels constitute the basic input information to set up a LISFLOOD run, whereas data on precipitation, air temperature, potential evapotranspiration, and evaporation from water bodies and bare soil surfaces are the main meteorological drivers. LISFLOOD was calibrated using at least four years of historical river flow data in the period 1995–2002 in 258 catchments and sub-catchments distributed throughout Europe (Feyen et al. 2008). LISFLOOD has been coupled offline with a 12-member ensemble of climate simulations under the A1B emission scenario (see Table S1) to simulate spatial and temporal patterns of catchment responses accounting for climate changes. For each climate experiment, 120 years of daily discharges (1981-2100) was produced at each river pixel (5 km horizontal resolution). Annual maximum river discharges were selected and a Gumbel distribution was fitted on time slices of thirty years. This distribution was used to obtain return periods between 2 and 500 years for each pixel and associated river discharges were converted to water depths using information on river channels (geometry) from the Catchment Information System (CIS) (Hiederer, R. and de Roo, A. 2003). A planar approximation, in which the flood wave associated to the given return level is considered a plane, was used to intersect water depths and a high resolution DEM to estimate flood inundation extent. Outcome of this procedure were inundation maps at 100 m horizontal resolution for different return periods and time slices. Low flows were identified through the magnitude of the river discharge, expressed by the 7-day minimum discharge. From the smoothed discharge, time series of annual minima were selected and a generalized extreme value distribution was fitted and used to retrieve streamflow droughts for different return periods ranging between 2 and 100 year in each pixel and for each time slice. Validation of both maximum river discharges and streamflow droughts and assessment of extreme value fitting uncertainty was performed on at least 446 gauging stations across Europe (Rojas et al. 2012; Forzieri et al. 2014). For this study we used simulations of river floods and streamflow droughts performed in previous works (Rojas et al. 2012; Rojas et al. 2013; Forzieri et al. 2014)

Text S2. Data harmonization

The coordinate system of the climate hazard indicators has been harmonized to the European Terrestrial Reference System 1989 in the Lambert Azimuthal Equal Area Projection and spatial resolution scaled to the common 1000-m grid. Figure S2 shows the spatial modeling domain for each hazard. Note that for river and coastal floods the baseline 500-yr flood

extension is used as reference modelling domains. Hazard-specific results grouped per European region are computed by including all pixels within the hazard modelling domain.

The local detail of our multi-hazard analysis should be viewed with caution because affected by the different modelling resolutions employed to reproduce the underlying physical processes (ranging between 25-km to 100-m grid cell, Text S1). Different spatial accuracies resulting from the different scales on which hazard-specific processes are simulated may influence the comparability amongst multi-resolution hazards and ultimately the level of detail resulting from their overlapping. However, we argue that the spatial detail of each single hazard is consistent with those documented in literature on which our multi-hazard exercise is built (Russo et al. 2014; Migliavacca et al. 2013a; Outten and Esau 2013; Pardaens et al. 2011; Cid et al. 2014; Rojas et al. 2012; Rojas et al. 2013; Forzieri et al. 2014).

Text S3. Overall Exposure Index

In order to quantify the total exposure resulting from the combination of multiple hazards we define the Overall Exposure Index (OEI). The method used for computing the OEI was inspired by the Hazus software tool developed by the U.S. Federal Emergency Management Agency for multi-hazard risk assessment. For clarity purposes we report an example of the Overall Exposure Index calculation in a simplified case with three hazards, whose expected annual fraction exposed are named A, B and C. Assuming that the hazards are compatible (non-exclusive) their EAFEs are treated as independent. This concept is graphically represented by the Venn diagrams in Figure S3, where each hazard is visualized by a circle whose area corresponds to its expected annual fraction exposed. The areas of intersection correspond to the overlapping of multiple hazards. Based on the aforementioned considerations, the OEI resulting from the combination of exposures of at least one single hazard is:

$$OEI_{1} = A + B + C - (A \cap B + A \cap C + B \cap C) + (A \cap B \cap C), \qquad [5]$$

that exactly corresponds to the formulation expressed in equation [3] in the main text.

The OEI resulting from the combination of exposures of two overlapping hazards is:

$$OEI_{2} = A \cap B + A \cap C + B \cap C - 2 \cdot A \cap B \cap C, \qquad [6]$$

The OEI resulting from the combination of exposures of three overlapping hazards is:

$$OEI_3 = A \cap B \cap C \,, \qquad [7]$$

The procedure is analogously replicated in the 7-hazard scenario considered in this paper and expressed in its general formulation:

$$OEI_m(T_R) = \bigcup_{\substack{J \subset \{1,\ldots,n\} \\ |J|=m}} EAFE_J(T_R)\,, \qquad [8]$$

where *m* refers to the number of overlapping hazards, *n* is the number of hazards considered, and the union operator runs over all subsets *J* of the indices *{1,…,n}* containing exactly m elements, and

$$EAFE_J(T_R) = \bigcap_{i \in J} EAFE_i(T_R)\,, \qquad [9]$$

denotes the intersection of all those $EAFE_i$ with index in *J*.

Equal weight is assigned to each hazard in the OEI metric. Then, for future scenarios an increase in a hazard can be fully compensated by a decrease of a similar magnitude of another hazard, leaving unaltered – in case of no change for the other hazards – the resulting future OEI. Analyses of OEI are performed for each baseline return period and time slice using the ensemble median of all climate model combinations for each hazard as input because only one single GCM-RCM configuration is in common amongst hazards. To understand the possible effects of climate uncertainty on multi-hazard metrics, OEIs have been also calculated by using the single-hazard grid-cell ensemble minimum and maximum as inputs.

OEI has been computed only for the spatial domain in common amongst hazards.

Text S4. Change Exposure Index

To identify areas subject to different levels of change to multiple hazards we define the Change Exposure Index (CEI). CEI expresses the number of hazards with a future relative increase in EAFE over a certain fixed threshold. We consider as reference 20%, 100% and 1000% relative increases (CEI_{20}, CEI_{100} and CEI_{1000}, respectively). The use of three different thresholds allows capturing moderate, strong and extreme changes in hazard exposure. The number of hazards with a change in exposure over the given threshold is calculated within

each grid cell and then aggregated at NUTS3 level regions. For regions with no NUTS3 available we refer to the NUTS0 level (see Figure S1). The 99th percentile of the exposure change distribution within the NUTS excludes local fitting extrapolation errors and is considered representative of the maximum degree of change in exposure and assigned to the whole region. CEI allows identifying key hotspots subject to predefined levels of change in exposure. To better assess the hazard-specific contributions to the CEI calculation, the afore-mentioned aggregation procedure is replicated separately for each hazard. This results in hazard-specific binary maps showing those regions experiencing a relative increase in Expected Annual Fraction Exposed larger than the fixed threshold for each specific hazard (Figure S6). Equal weight is assigned to each hazard in the CEI metric. Compensatory effects are effective if EAFEs of different hazards balance exceeding and falling behind the given threshold.

Similarly to OEI, analyses of CEI are performed for each return level and time slice using the ensemble median and minimum/maximum of EAFE of all climate model combinations for each hazard as input, limited to the spatial domain in common amongst hazards.

References

Cid A, Castanedo S, Abascal AJ, et al (2014) A high resolution hindcast of the meteorological sea level component for Southern Europe: the GOS dataset. Clim Dyn 43:2167–2184. doi: 10.1007/s00382-013-2041-0

Dosio A, Paruolo P (2011) Bias correction of the ENSEMBLES high-resolution climate change projections for use by impact models: Evaluation on the present climate. J Geophys Res Atmospheres 116:D16106. doi: 10.1029/2011JD015934

Egbert GD, Erofeeva SY (2002) Efficient Inverse Modeling of Barotropic Ocean Tides. J Atmospheric Ocean Technol 19:183–204. doi: 10.1175/1520-0426(2002)019<0183:EIMOBO>2.0.CO;2

European Commission (2008) Forest fires in Europe 2008. JRC Scientific and Technical Report

Feyen L, Kalas M, Vrugt JA (2008) Semi-distributed parameter optimization and uncertainty assessment for large-scale streamflow simulation using global optimization / Optimisation de paramètres semi-distribués et évaluation de l'incertitude pour la simulation de débits à grande échelle par l'utilisation d'une optimisation globale. Hydrol Sci J 53:293–308. doi: 10.1623/hysj.53.2.293

Forzieri G, Feyen L, Rojas R, et al (2014) Ensemble projections of future streamflow droughts in Europe. Hydrol Earth Syst Sci 18:85–108. doi: 10.5194/hess-18-85-2014

Giglio L, Randerson JT, van der Werf GR, et al (2010) Assessing variability and long-term trends in burned area by merging multiple satellite fire products. Biogeosciences 7:1171–1186. doi: 10.5194/bg-7-1171-2010

Haidvogel DB, Arango H, Budgell WP, et al (2008) Ocean forecasting in terrain-following coordinates: Formulation and skill assessment of the Regional Ocean Modeling System. J Comput Phys 227:3595–3624. doi: 10.1016/j.jcp.2007.06.016

Hendrik Tolman MA (2014) User manual and system documentation of WAVEWATCH III version 4.18.

Hiederer, R., de Roo, A. (2003) A european flow network and catchment data set. European Commission, Joint Research Centre

Jakob Themeßl M, Gobiet A, Leuprecht A (2011) Empirical-statistical downscaling and error correction of daily precipitation from regional climate models. Int J Climatol 31:1530–1544. doi: 10.1002/joc.2168

Kloster S, Mahowald NM, Randerson JT, et al (2010) Fire dynamics during the 20th century simulated by the Community Land Model. Biogeosciences 7:1877–1902. doi: 10.5194/bg-7-1877-2010

Migliavacca M, Dosio A, Camia A, et al (2013a) Modeling biomass burning and related carbon emissions during the 21st century in Europe. J Geophys Res Biogeosciences 118:2013JG002444. doi: 10.1002/2013JG002444

Migliavacca M, Dosio A, Kloster S, et al (2013b) Modeling burned area in Europe with the Community Land Model. J Geophys Res Biogeosciences 118:265–279. doi: 10.1002/jgrg.20026

Outten SD, Esau I (2013) Extreme winds over Europe in the ENSEMBLES regional climate models. Atmos Chem Phys 13:5163–5172. doi: 10.5194/acp-13-5163-2013

Pardaens AK, Lowe JA, Brown S, et al (2011) Sea-level rise and impacts projections under a future scenario with large greenhouse gas emission reductions. Geophys Res Lett 38:L12604. doi: 10.1029/2011GL047678

Reguero BG, Menéndez M, Méndez FJ, et al (2012) A Global Ocean Wave (GOW) calibrated reanalysis from 1948 onwards. Coast Eng 65:38–55. doi: 10.1016/j.coastaleng.2012.03.003

Rojas R, Feyen L, Bianchi A, Dosio A (2012) Assessment of future flood hazard in Europe using a large ensemble of bias-corrected regional climate simulations. J Geophys Res Atmospheres 117:D17109. doi: 10.1029/2012JD017461

Rojas R, Feyen L, Dosio A, Bavera D (2011) Improving pan-European hydrological simulation of extreme events through statistical bias correction of RCM-driven climate simulations. Hydrol Earth Syst Sci 15:2599–2620. doi: 10.5194/hess-15-2599-2011

Rojas R, Feyen L, Watkiss P (2013) Climate change and river floods in the European Union: Socio-economic consequences and the costs and benefits of adaptation. Glob Environ Change 23:1737–1751. doi: 10.1016/j.gloenvcha.2013.08.006

Russo S, Dosio A, Graversen RG, et al (2014) Magnitude of extreme heat waves in present climate and their projection in a warming world. J Geophys Res Atmospheres 119:12,500–12,512. doi: 10.1002/2014JD022098

Russo S, Sillmann J, Fischer EM (2015) Top ten European heatwaves since 1950 and their occurrence in the coming decades. Environ Res Lett 10:124003. doi: 10.1088/1748-9326/10/12/124003

Saha S, Moorthi S, Pan H-L, et al (2010) The NCEP Climate Forecast System Reanalysis. Bull Am Meteorol Soc 91:1015–1057. doi: 10.1175/2010BAMS3001.1

Solomon S (2007) Climate Change 2007 - The Physical Science Basis: Working Group I Contribution to the Fourth Assessment Report of the IPCC. Cambridge University Press

Van Der Knijff JM, Younis J, De Roo APJ (2010) LISFLOOD: a GIS-based distributed model for river basin scale water balance and flood simulation. Int J Geogr Inf Sci 24:189–212. doi: 10.1080/13658810802549154

van der Werf GR, Randerson JT, Giglio L, et al (2010) Global fire emissions and the contribution of deforestation, savanna, forest, agricultural, and peat fires (1997–2009). Atmos Chem Phys 10:11707–11735. doi: 10.5194/acp-10-11707-2010

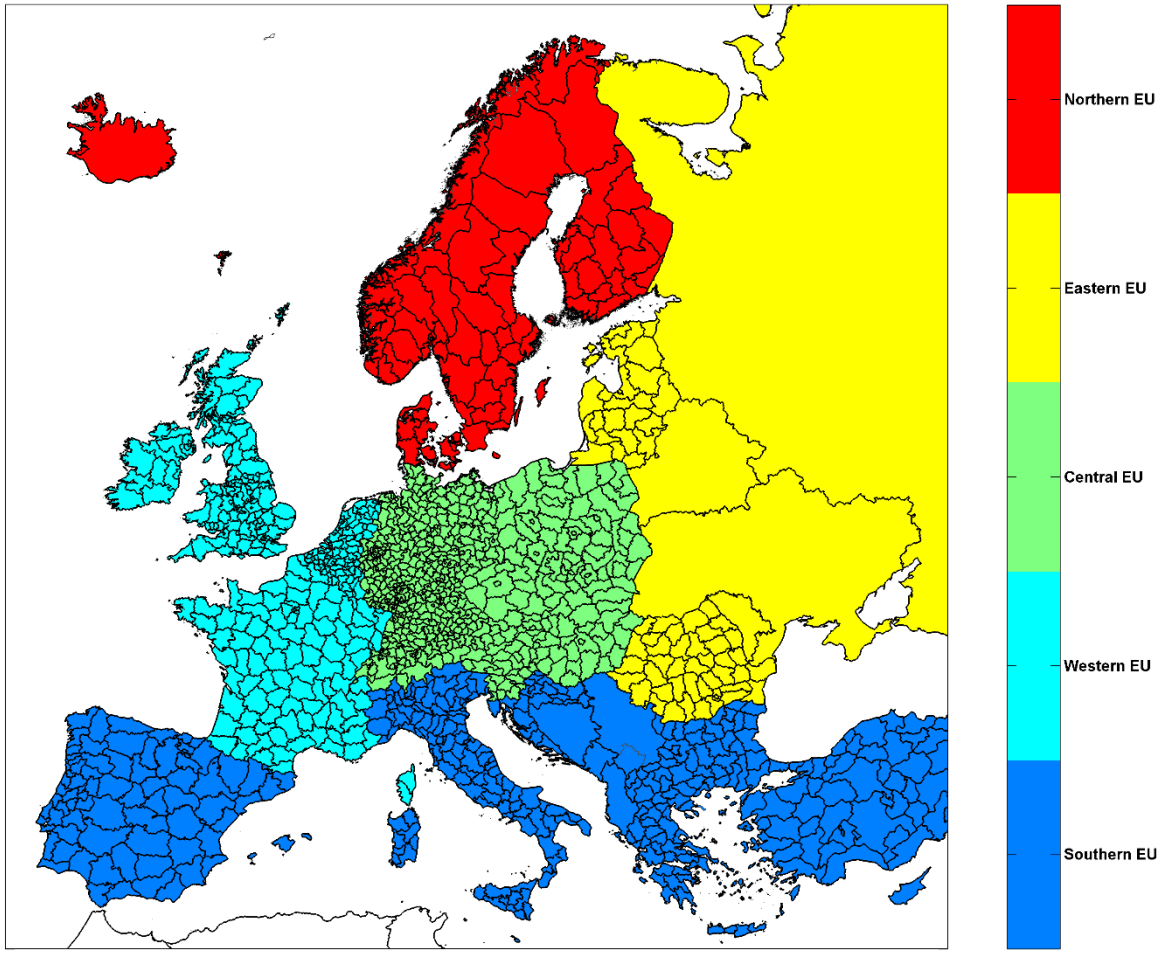

Fig S1 European regions. Grouping of countries in macro-areas shown in different colors and NUTS3 regions visualized in black line polygons. Southern Europe (Albania, Bulgaria, Bosnia and Herzegovina, Croatia, Cyprus, Greece, Italy, Kosovo, Malta, Montenegro, Portugal, Republic of Macedonia, Serbia, Slovenia, Spain, Turkey), Central Europe (Austria, Czech Republic, Germany, Liechtenstein, Poland, Switzerland), Western Europe (Belgium, France, Ireland, Netherlands, Luxembourg, United Kingdom), Eastern Europe (Belarus, Estonia, Hungary, Latvia, Lithuania, Republic of Moldova, Romania, Russian Federation, Slovakia, Ukraine), and Northern Europe (Denmark, Iceland, Finland, Norway, Sweden).

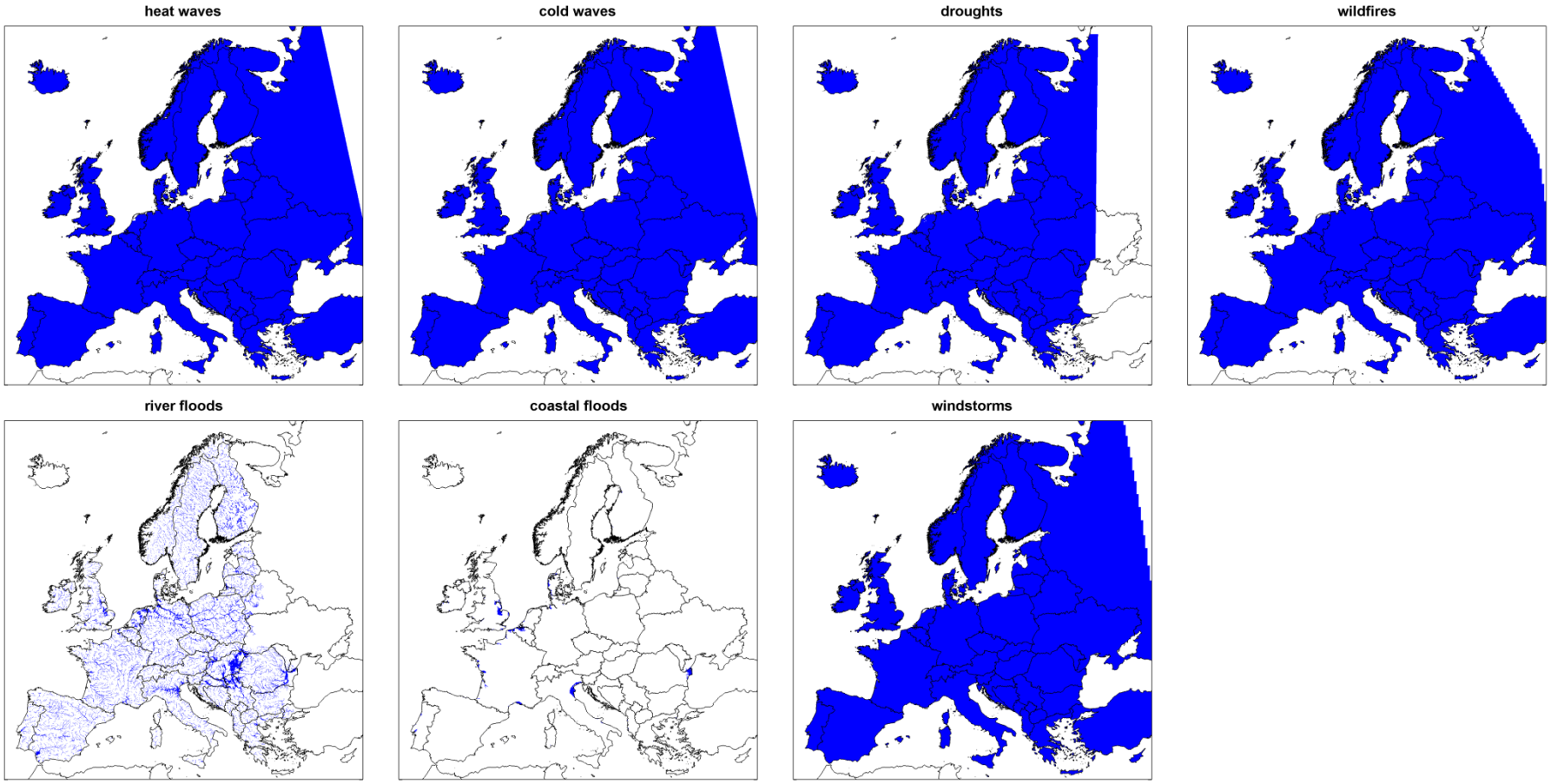

Fig S2 Spatial domains of climate hazard models.

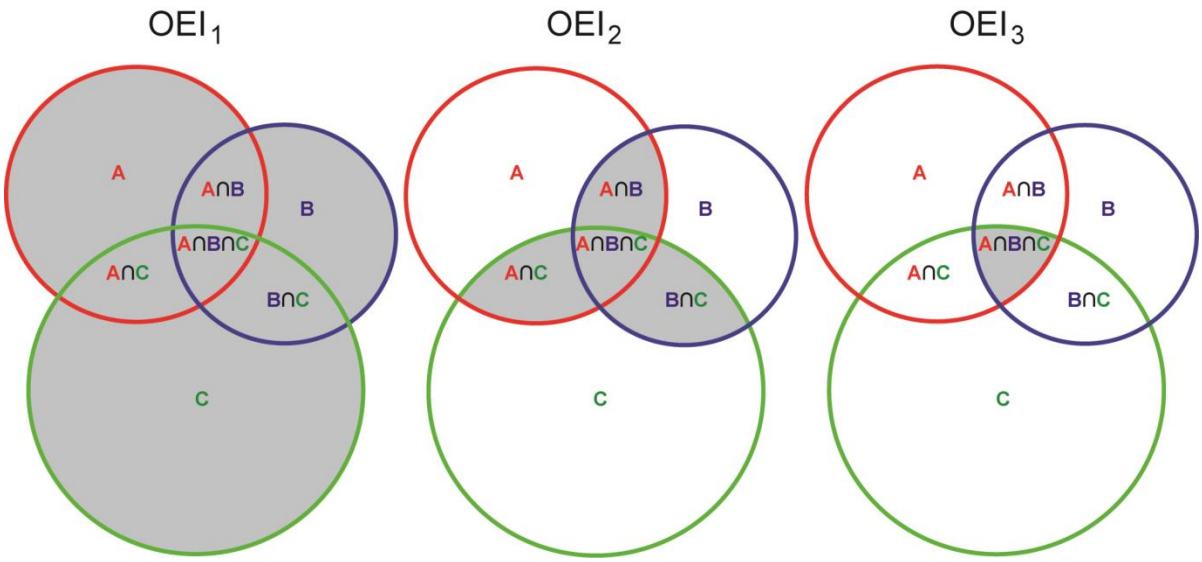

Fig S3 Schema of calculation of Overall Exposure Index. Example of calculation of Overall Exposure Index in a simplified case with three hazards, here visualized by colored circles, named A, B and C, respectively. Gray areas represent the Overall Exposure Index with different degree of overlapping.

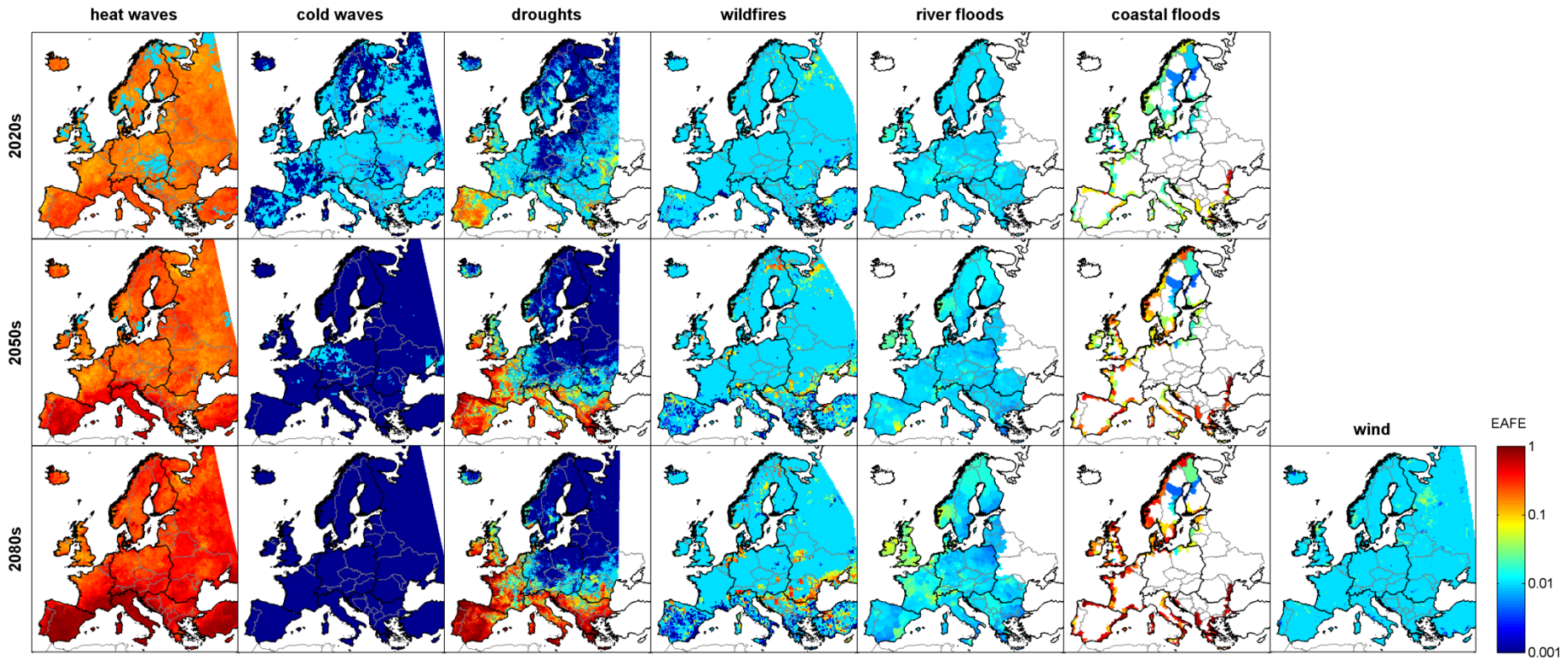

Fig S4 Spatio-temporal patterns of 100-yr Expected Annual Fraction Exposed. Spatial and temporal variations of Expected Annual Fraction Exposed to 100-yr climate hazards. Note that values for river and coastal floods are aggregated at NUTS3 level (see Fig. S1) to better visualize their effects. Values refer to the ensemble medians of experiments driven by the available climate models.

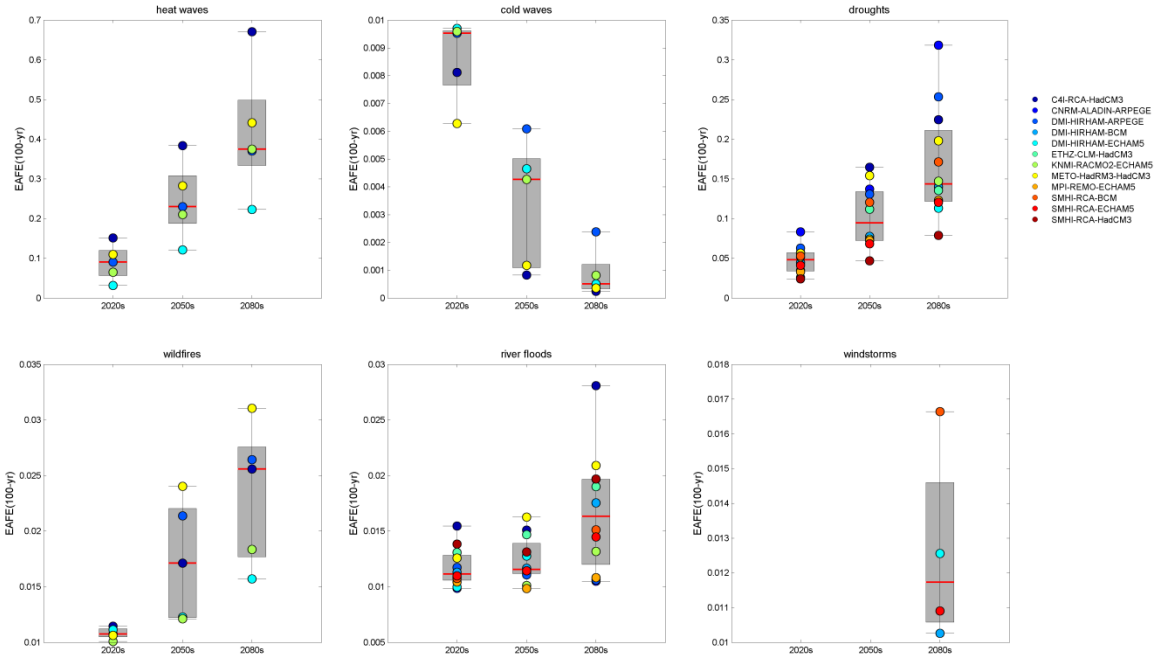

Fig S5 Inter-model spread of 100-yr Expected Annual Fraction Exposed aggregated at Europe level. Coloured circles refer to EAFEs obtained by specific climate model realizations, gray boxes extent from the first and third inter-quartiles of the ensemble distribution, black whiskers are the upper and lower values, red line is the median.

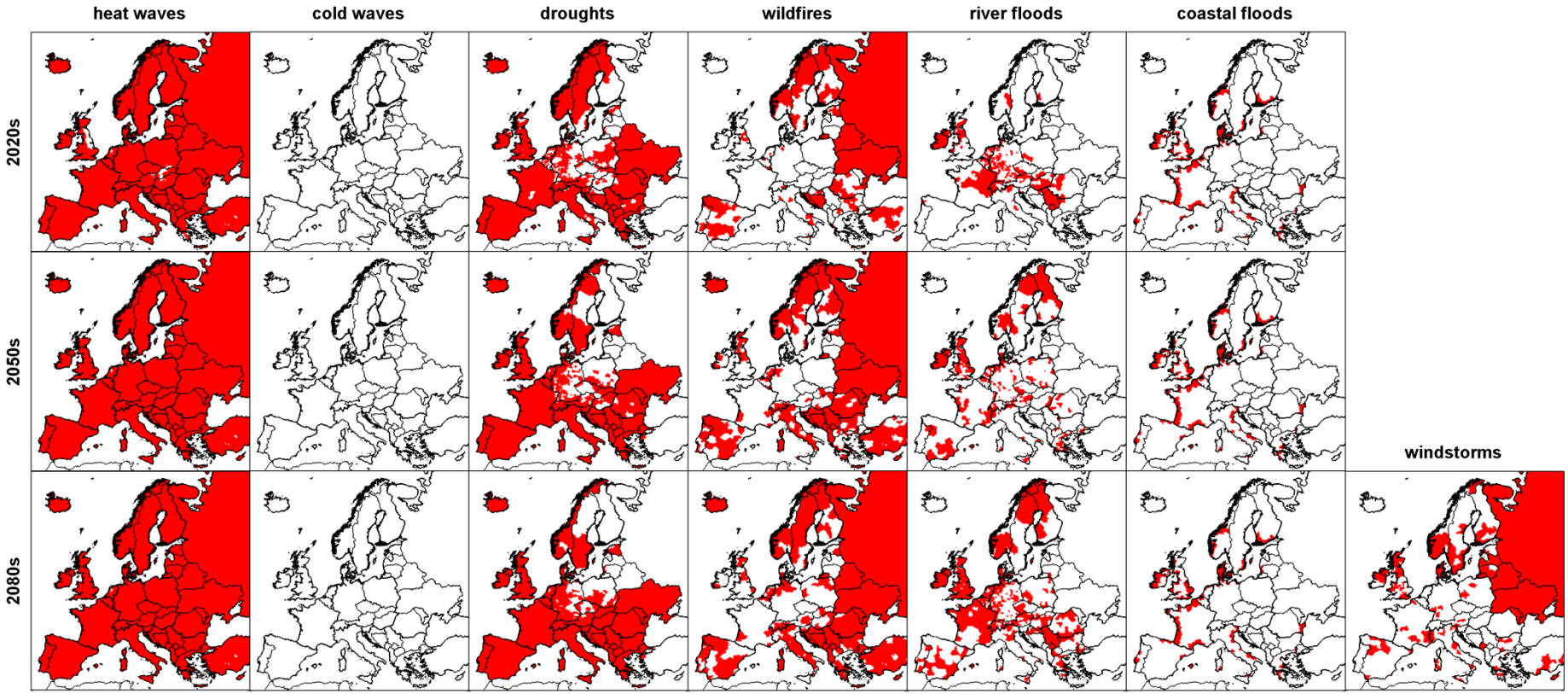

Fig S6 Hazard-specific contributions to the Change Exposure Index calculation. NUTS3 regions whose relative increase in 100-yr Expected Annual Fraction Exposed is larger than the fixed 20% (in red).

Driving GCM	RCM	Acronyms	Heat waves	Cold waves	Droughts	Wildfires	River floods	Windstorms
HadCM3Q16	RCA3.0	C4I-RCA-HadCM3	X	X	X	X	X	
ARPEGE	ALADIN-RM5.1	CNRM-ALADIN-ARPEGE			X		X	
ARPEGE	HIRHAM5	DMI-HIRHAM5-ARPEGE	X	X	X	X	X	
BCM	HIRHAM5	DMI-HIRHAM5-BCM			X		X	X
ECHAM5-r3	HIRHAM5	DMI-HIRHAM5-ECHAM5	X	X	X	X	X	X
HadCM3Q0	CLM	ETHZ-CLM-HadCM3			X		X	
ECHAM5-r3	RACMO2	KNMI-RACMO2-ECHAM5	X	X	X	X	X	
HadCM3Q0	HadRM3Q0	METO-HadRM3-HadCM3	X	X	X	X	X	
ECHAM5-r3	REMO	MPI-REMO-ECHAM5			X		X	
BCM	RCA3.0	SMHI-RCA-BCM			X		X	X
ECHAM5-r3	RCA3.0	SMHI-RCA-ECHAM5			X		X	X
HadCM3Q3	RCA3.0	SMHI-RCA-HadCM3			X		X	

Tab S1 Climate simulations used to derive climate hazard indicators in the period 1981–2100.